# A parameterization scheme for the floating wind farm in a coupled atmosphere-wave model (COAWST v3.7)

Shaokun Deng[1], Shengmu Yang[2], Shengli Chen[1], Xuefeng Yang[1], Shanshan Cui[1]

[1]Institute for Ocean Engineering, Shenzhen International Graduate School, Tsinghua University, Shenzhen, China
[2]College of Meteorology and Oceanography, National University of Defense Technology, Changsha, China

*Correspondence to*: Shengli Chen (shenglichen@sz.tsinghua.edu.cn)

**Abstract.** Coupling Weather Research and Forecasting (WRF) model with wind farm parameterization can be effective in examining the performance of large-scale wind farms. However, the current scheme is not suitable for floating wind turbines. In this study, a new scheme is developed for floating wind farm parameterization (FWFP) in the WRF model. The impacts of the side columns of a semi-submersible floating wind turbine on waves are firstly parameterized in the spectral wave model (SWAN) where the key idea is to consider both inertial and drag forces on side columns. A machine learning model is trained using results of idealized high-resolution SWAN simulations and then implemented in the WRF to form the FWFP. The difference between our new scheme and the original scheme in a realistic case is investigated using a coupled atmosphere-wave model. Results indicate that the original scheme underestimates the power output of the entire floating wind farm in the winter scenario. On average, the power output of a single turbine is underestimated by a maximum of 694 kW (12 %). The turbulent kinetic energy decreases within the wind farm, with the greatest drop of 0.4 $m^2 s^{-2}$ at the top of the turbine. This demonstrates that the FWFP is necessary for both predicting the power generated by floating wind farms and evaluating the impact of floating wind farms on the surrounding environment.

## 1 Introduction

Wind energy has demonstrated great development potential in recent years. The number of wind farms that have been built is enormous, and there are predictions that wind power generation will be on the rise in the future. (Pryor et al., 2020). The pre-assessments of wind farms are not suitable to be investigated with the computational fluid dynamics (CFD) models and large-eddy simulation (LES) model due to great computational expense and feedback effects that cannot be captured by high-resolution non-meteorological microscale models alone. The relevant physical processes, which are important for large wind farms, are also not included in the engineering wake models (Emeis, 2010). Currently, an important tool for examing large-scale wind sources and wake interferences is mesoscale model with a wind farm parameterization.

There are two different methods to parameterize the wind farm in mesoscale models: implicit and explicit methods. Previous results have shown that explicit methods present a more physically consistent representation of wind farm effects and result in more realistic simulations (Fitch et al., 2013; Fitch, 2015). The explicit methods also have the advantage of taking info account how wind speeds interact with the lower surface (Du et al., 2017; Vanderwende and Lundquist, 2016). The explicit methods parameterize the wind farm effect as a momentum sink on the mean flow Most of parameterizations are conducted in the free, open-source Weather Research and Forecasting (WRF) model, which already includes the Fitch wind farm parameterization in its release (Fitch et al., 2012). The original Fitch scheme has been the subject of a number of recent developments and modifications. Most of studies have focused on sub-grid effects of wind turbines (Abkar and Porte-Agel, 2015; Ma et al., 2022a,b; Pan and Archer, 2018; Redfern et al., 2019). The installed capacity of offshore wind energy has been continuously increasing (Diaz, 2020). The global offshore wind power development is moving from offshore to deeper waters, where floating offshore wind turbines have advantage over bottom fixed offshore wind turbines in water depths greater than 50 m (Diaz, 2020; Roddier et al., 2010). Floating offshore wind turbines can have a substantial impact on waves due to floating platforms, which in turn leads to major changes in roughness length of ocean surface. Changes in the roughness length in turn affect the wind field through momentum transfer between the atmosphere and the waves. And the effect of the wave field on the wind field can reach up to the height of the turbine, according to previous studies (AlSam et al., 2015; Jenkins et al., 2012; Kalvig et al., 2014; Paskyabi et al., 2014; Porchetta et al., 2021; Wu et al., 2020; Yang et al., 2014; Zou et al., 2018). This suggests that the current wind farm parameterization is not suitable for floating wind farms because it does not account for the change in roughness length caused by large floating platforms.

In contrast to studies investigating the influence of offshore wind farm wake on waves, few studies have investigated the influence of wind farm structures (piles) on waves through the effects of drag dissipation. Ponce de Leon et al. (2011) used a wave model to study the impact of an offshore wind farm on nearby waves. They represented each monopile foundation as a dry point (land) in the model. They found that the method blocked the propagation of the wave energy and caused a slight change in the direction of the wave. Alari and Raudsepp (2012) found that the impact of the wind turbine on the significant wave height (SWH) was very marginal, with changes of the SWH smaller than 1 % at areas shallower than 10 m depth. Molen et al. (2014) conducted sensitivity experiments to study the influence of turbine spacing and size of wind farm on the SWH, and found that the SWH could be reduced by up to 9.58 %. McCombs et al. (2014) evaluated the impact of an offshore wind farm on waves in Lake Ontario using a coupled wave-hydrodynamic model. In contrast to previous studies, they simulated the offshore wind farm with the application of a transmission coefficient in the wave model. The results indicated that with changes in SWH predicted to be less than 3 %. These previous studies simulate the wind turbine in the model as a dry grid point, which has two limitations, 1) the model resolution is too high to implement for large-scale offshore wind farm scenarios, 2) it can only represent the diffraction effects, however, wave forces include drag and inertial forces (Isaacson, 1979; Morison et al., 1950). By parameterizing both the drag and inertial forces in the numerical model, the impact of the offshore wind turbine/farm on the waves can be analyzed more accurately.

In this study, a floating wind farms parameterization (FWFP) scheme in the WRF Model is developed to represent the effect of the offshore wind farm on surface waves. In Section 2, the wave energy dissipation due to the inertial forces of waves is implemented in SWAN. The model configuration and results of high-resolution idealized simulations are presented in Section 3. In Section 4, we propose a machine learning module used to fit the effect of wave inertial forcings represented in high-resolution SWAN simulations. Section 5 describes how the floating wind farm parameterization scheme is implemented in the WRF, and presents the results and the analysis of the wind speed deficit, power output, and the influence of the new scheme on the turbulent kinetic energy. The conclusion is given in Section 6.

## 2 Parameterization of the wave inertial force in SWAN

SWAN is a third-generation phase-averaged spectral wave model (Booij et al., 1999). SWAN has a function to account for wave damping over a vegetation (VEG) at variable depths. The cylinder approach proposed by Dalrymple et al. (1984) is a well-known method for expressing wave dissipation due to vegetation. In this approach, the energy loss is calculated based on the actual work done by the force of the plant on the fluid, expressed by the Morrison equation. Two modifications convert the VEG module into the semi-submersible floating wind turbine module. The first modification then is that the module only needs to calculate the results of Sveg,3 (the red dashed box in Figure 1) and set d (column draft depth) to a constant (d=20 m is used in this paper).

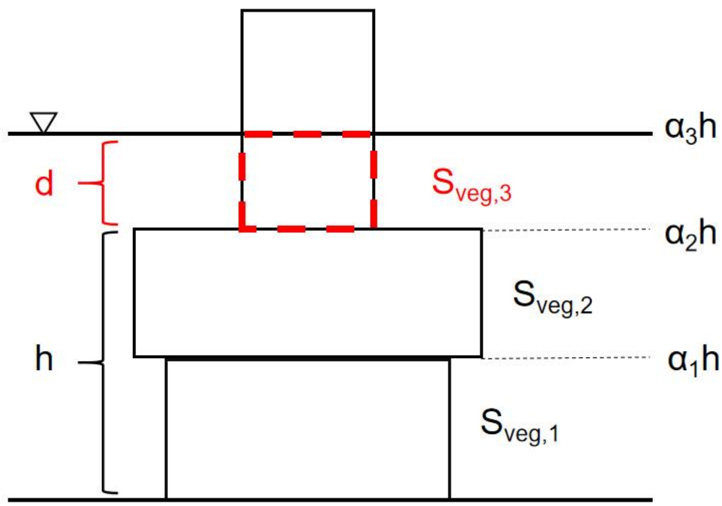


**Figure 1.** Layer schematization for vegetation

Another important modification of the VEG module concerns the energy dissipation due to wave forces. In the VEG module, the wave force is derived from the drag force in a Morison type equation with the inertial forces neglected. Since the vegetation is assumed to be a cylinder with a small diameter, the drag force is considered to be dominant. However, for the floating offshore wind turbine, the diameter of the cylinder cannot be neglected compared to the wavelength. The wave forces become more complex and require the consideration of inertial forces. The equation for the energy dissipation due to inertial forces can be derived from the work of Morison et al. (1950).

$$D = \int_{-(h+d)}^{-h} F_{iner} u dz = \int_{-(h+d)}^{-h} \rho C_M \frac{\pi}{4} b^2 \frac{\partial u}{\partial t} u dz, \quad (1)$$

where $C_M$ is the inertial force coefficient, $b$ is the cylinder diameter. Based on Kobayashi et al. (1993),

$$u = \frac{gkH}{2\omega}\frac{\cosh[k(h+d+z)]}{\cosh[k(h+d)]}, \tag{2}$$

$$\frac{\partial u}{\partial t} = \frac{gkH}{2}\frac{\cosh[k(h+d+z)]}{\cosh[k(h+d)]}[\delta c_2 + (\delta - \varepsilon)c_3], \tag{3}$$

where $\omega$ is the wave angular frequency, $H$ is the wave height, $k$ is the wave number, $h$+$d$ is the water depth, $d$ is the draft depth (Figure 1).

The equations for the other parameters are as follows,

$$\varepsilon = \frac{C_D bH}{9\pi}c_5, \tag{4}$$

$$\delta = \varepsilon c_4, \tag{5}$$

$$c_2 = \frac{\sinh kh \sinh[k(h+d)] - kh \tanh kd}{\cosh kd}, \tag{6}$$

$$c_3 = k(h+d+z)\tanh[k(h+d+z)] - kd \tanh kd, \tag{7}$$

$$c_4 = \frac{2kd + \sinh 2kd}{2k(h+d) + \sinh[2k(h+d)]}, \tag{8}$$

$$c_5 = \frac{\sinh 3kd + 9\sinh kd}{(2kd + \sinh 2kd)\sinh[k(h+d)]}, \tag{9}$$

Substitution of Eqs. (2), (3) and (7) into Eq. (1) yields

$$D = \frac{\rho C_M \pi b^2 k(gH)^2}{16\omega[\cosh k(h+d)]^2}\left[\delta c_2 \frac{\sinh 2kd + 2kd}{4} + (\delta - \varepsilon)\frac{2kd\cosh 2kd - \sinh 2kd - kd\tanh kd(\sinh 2kd + 2kd)}{8}\right], \tag{10}$$

Substitution of Eqs. (4) and (5) into Eq. (10) yields

$$D = \frac{\rho C_M C_D b^3 k g^2 H^3}{144\omega[\cosh k(h+d)]^2}\left[c_2 c_4 c_5 \frac{\sinh 2kd + 2kd}{4} + c_5(c_4 - 1)\frac{2kd\cosh 2kd - \sinh 2kd - kd\tanh kd(\sinh 2kd + 2kd)}{8}\right], \tag{11}$$

The Rayleigh probability density function is related to wave height (Mendez and Losada, 2004),

$$H^3 = \int_0^\infty H^3 p(H)\,dH, \tag{12}$$

$$\int_0^\infty H^3 p(H)\,dH = \frac{3\sqrt{\pi}}{4}H_{rms}^3, \tag{13}$$

where $p(H)$ is the Rayleigh probability density function, $H_{rms}$ is the root-mean-square wave height. Substitution of Eqs. (12) and (13) into Eq. (11) and dividing by the bulk density of the fluid yields

$$D = \frac{\rho C_M C_D b^3 gk}{144\omega[\cosh k(h+d)]^2}\frac{3\sqrt{\pi}}{4}H_{rms}^3\left[c_2c_4c_5\frac{\sinh 2kd+2kd}{4} + c_5(c_4-1)\frac{2kd\cosh 2kd - \sinh 2kd - kd\tanh kd(\sinh 2kd+2kd)}{8}\right], \tag{14}$$

The root-mean-square wave height and the total wave energy have such a relationship, $H_{rms}^2 = 8E_{tot}$, and substituting it into Eq. (14) yields,

$$D = \frac{1}{8}\sqrt{\frac{\pi}{72}}\frac{C_M C_D b^3 gk}{\omega[\cosh k(h+d)]^2}\left[2c_2c_4c_5(\sinh 2kd + 2kd) + c_5(c_4-1)[2kd\cosh 2kd - \sinh 2kd - kd\tanh kd(\sinh 2kd + 2kd)]\right]E_{tot}^{3/2}, \tag{15}$$

Eq. (15) is the equation calculating the energy dissipation due to the inertial force. In the study, the magnitudes of the inertial force and the drag force are calculated and compared for the cylinders with diameters of 10 m and 1 m.

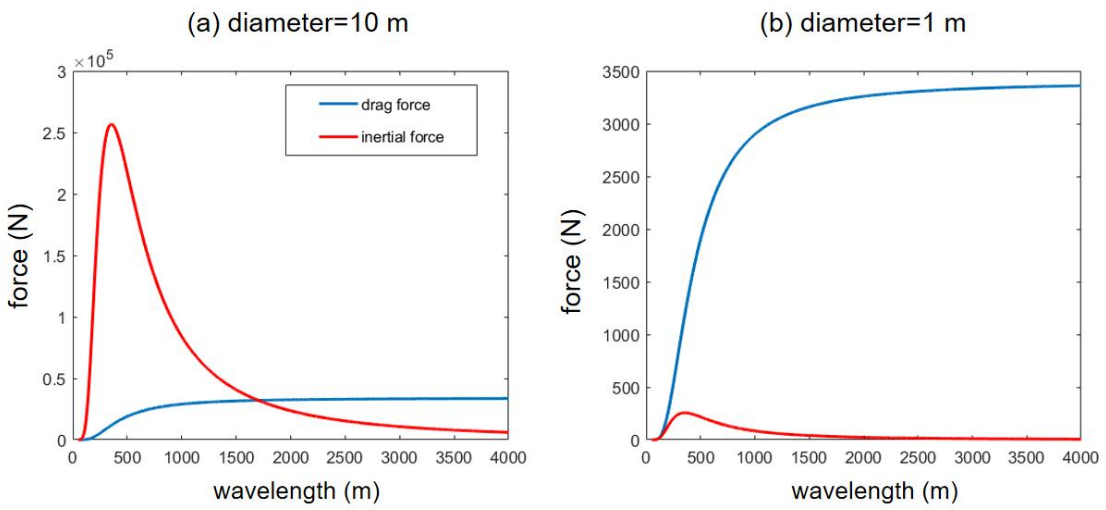


**Figure 2.** Inertial forces (red solid line) and drag forces (blue solid line) for cylindrical diameters of (a) 10 m and (b) 1 m (incident wave height of 3 m, drag coefficient of 1.2, draft depth of 20 m, water depth of 80 m)

The case is set with the incident SWH of 3 m, the drag coefficient of 1.2, the draft depth of 20 m, and the water depth being 80 m. When the cylinder diameter is 10 m (Figure 2a), the average wavelength of the incident wave is within 1700 m, which makes the inertial force larger than the drag force. However, when the cylinder diameter is 1 m (Figure 2b), the inertial force is always smaller than the drag force. As the wavelength increases (the scale becomes smaller), the drag force becomes larger relative to the inertial force, which is consistent with the assumption of the VEG module that the inertial force could be neglected, but the inertial force can not be ignored for the side column of the floating offshore wind turbine. Thus the VEG module in SWAN is modified to include the inertial force to be applicable for the floating wind turbine.

## 3 Idealized high-resolution simulations

As shown in Section 2, the floating offshore wind turbine module is developed for SWAN, and its impact on waves is examined using high-resolution numerical experiments in this section.

The rectangular domain of the idealized high-resolution experiments is shown in Figure 3, with 100 × 200 cells, a horizontal resolution corresponding to the column diameter of 10 m, and a water depth of 50 m. The position of the column is at the center of the computational domain. The incident SWH is 3 m, the mean wave period is 12 s, propagating from east to west, and the shape of the spectra is from the JONSWAP spectrum. Because of the small computational domain, the model uses stationary computation which converges after several time steps.

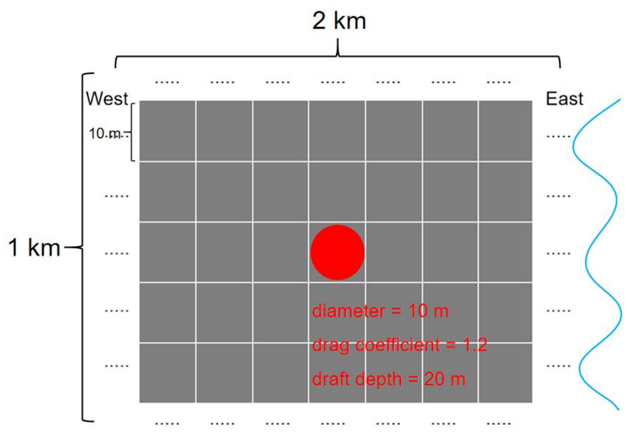


**Figure 3.** Experimental design of high-resolution idealized simulations (SWH=3 m, mean wave period=12 s, and depth=50 m)

Two experiments are conducted, one to study the influence of the column on the waves caused only by the drag force (ExpDragS), and the other to examine the influence caused by both the drag force and the inertial force (ExpInerS). It can be noted that when the energy dissipation is caused by the drag force only, the SWH attenuation is only ~0.2 m (Figure 4a), and the "wake" phenomenon occurs in the wave field. The angle of the mean wave direction is shifted by about 1° around the column and the horizontal distribution is symmetrical along the axis y=0 (Figure 4d). The mean wave length is increased by about 10 m (Figure 4g). When the inertial forces are taken into account, the energy dissipation is larger, which makes the SWH attenuation more significant, which is about 1.4 m (Figure 4b), indicating an attenuation of 50 % SWH. The mean wave direction deviation around the column is also relatively large, reaching about 5° (Figure 4e), and the mean wave length is about 24 m longer (Figure 4i) than that of ExpDragS.

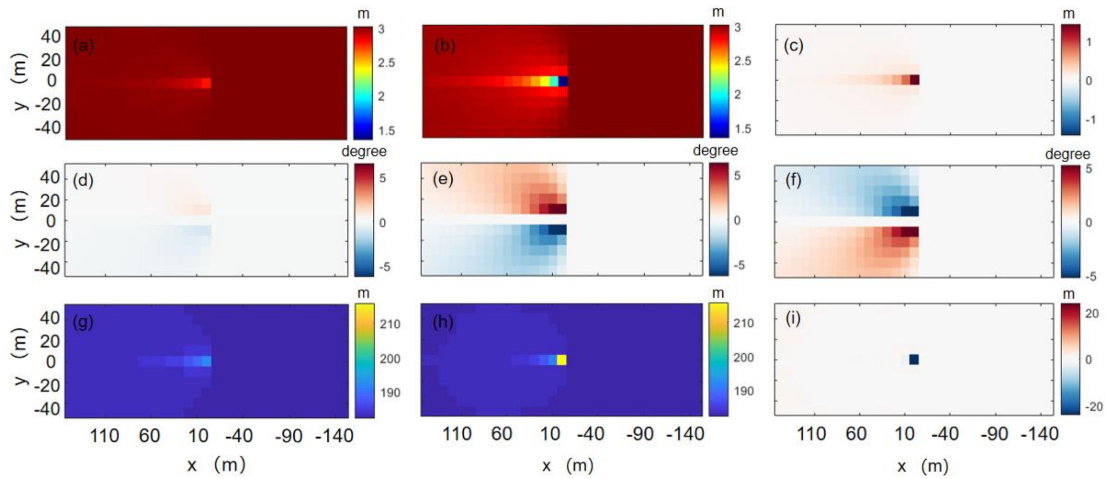


**Figure 4.** Significant wave height of (a) ExpDragS and (b) ExpInerS, (c) difference in significant wave height, (d) mean wave direction deviation of ExpDragS and (e) ExpInerS, (f) difference in mean wave direction deviation, (g) mean wave length of ExpDragS, and (h) ExpInerS, (i) difference in mean wave length

## 4 Machine learning parameterization

The results of the idealized high-resolution SWAN simulations in Section 3 show the impact of the floating offshore wind turbine's side columns on the waves, including the SWH attenuation, symmetrical changes of mean wave direction, and an increase in the mean wave length. However, it is computationally expensive to run a ~10 m resolution SWAN model.

Using Machine Learning (ML) to better parameterize unresolved processes in mesoscale and climate models has received much attention in recent years (O'Gorman and Dwyer, 2018; Gettelman et al., 2020; Seifert and Rasp, 2020). With the rise of scientific ML and its widespread use in the geosciences, the design of parametrizations using ML algorithms has become a trend in model development. To build an appropriate model, a large amount of data is needed for training. Nevertheless, the observational data on the impact of the floating offshore wind turbine on waves are scarce. As a result, the outputs of the high-resolution SWAN simulations in Section 3 are employed to train the ML model.

From the equations in Section 2, we can note that when the inertial force coefficient, drag force coefficient, and cylindrical diameter are determined, the energy dissipation caused by the wave force is only related to the water depth, incident SWH, and mean wave period (or peak period). We design a series of ideal experiments with different water depths, incident SWH, and mean wave periods. The SWH is taken from 2 m to 12 m with 1 m interval. The peak wave period is from 7 s to 12 s with an interval of 1 s, and the water depth is selected from 53 m to 98 m with an interval of 5 m. This has a total number of 660 (11 × 6 × 10) experimental groups. We then use these model data to train several machine learning (regression) models with the input of incident SWH, water depth, and peak wave period, and the output of SWH after energy dissipation. These models can be classified into four main categories: linear regression models, tree models, support vector machines (SVM), and Gaussian process regression (GPR). As shown in Figure 5, the GPR model with the Matern 5/2 kernel (covariance) function is the most reasonable, with a minimum root mean square error (RMSE) of 0.0096 m (Figure 5d). The model can be coupled with CFD, LES models and mesoscale meteorological models to predict the effect of the floating offshore wind turbine side columns on waves without the need for high-resolution SWAN simulations.

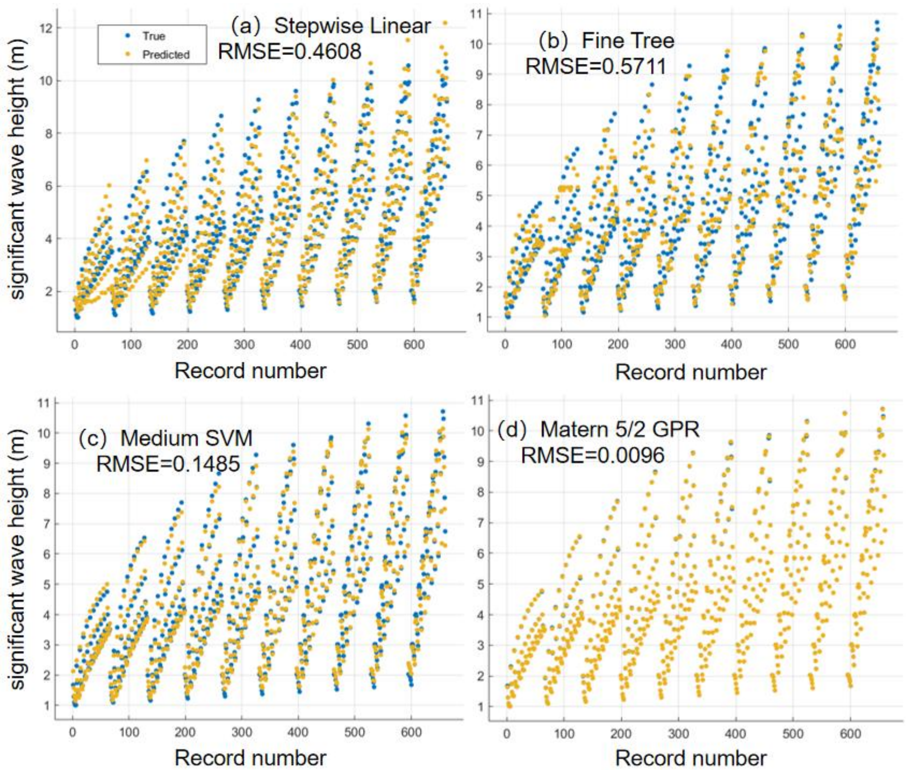


**Figure 5.** Response results of four typical regression models: (a) Stepwise linear regression (b) Fine tree (c) Medium SVM (d) Matern 5/2 Gaussian process regression

## 5 Parameterization in the WRF model

### 5.1 Implementation of parameterization in the WRF model

The important point in the derivation of the original wind farm parameterization equation is that the rate of kinetic energy loss in the grid cell is equal to the kinetic energy loss due to the wind turbine in the grid,

$$-\frac{1}{2}N_{ij}\Delta x\Delta y\rho C_T V_{ijk}^3 A_{ijk} = \Delta x\Delta y(z_{k+1}-z_k)\rho V_{ijk}\frac{\partial V_{ijk}}{\partial t}, \tag{16}$$

where $V_{ijk}$, is the horizontal wind speed, $N_{ij}$ is the number of turbines per square meter, $\rho$ is the air density, $C_T$ is the thrust coefficient of a wind turbine, $\Delta x$, $\Delta y$, are the horizontal grid size in the zonal and meridional directions respectively, $z_k$ is the height at model level k, $A_{ijk}$ is the cross-sectional rotor area of one wind turbine bounded by model levels k, $k+1$ in grid cell i, j.

For a semi-submersible floating wind turbine, the SWH around the turbine is considerably affected. As a result, the roughness of ocean surface nearby is also changed. The change in the kinetic energy due to changes in the momentum flux in the surface layer should be taken into account for the loss of kinetic energy in the grid cell. Therefore, in the simulation with semi-submersible floating wind turbines applied, Eq. (16) can be modified

$$-\frac{1}{2}N_{ij}\Delta x\Delta y[\rho C_T V_{ijk}^3 A_{ijk} - \Delta\tau S V_{ijk}(z_{k+1} - z_k)] = \Delta x\Delta y(z_{k+1} - z_k)\rho V_{ijk}\frac{\partial V_{ijk}}{\partial t}, \tag{17}$$

where $S$ is the area occupied by the floating platform. $\Delta\tau = \rho(u_{*,wt}^2 - u_*^2)$ is the change in the momentum flux due to the turbine. $u_{*,wt}$ is the frictional velocity at location of the turbine and $u_*$ is the frictional velocity unaffected by the turbine. A new equation for the momentum tendency term is given as

$$\frac{\partial V_{ijk}}{\partial t} = \frac{N_{ij}[\frac{1}{2}C_T V_{ijk}^2 A_{ijk} + (u_{*,wt}^2 - u_*^2)S(z_{k+1} - z_k)]}{z_{k+1} - z_k}, \tag{18}$$

It should be noted that Eq. (18) applies only to the heights between the bottom of the rotor area and 100 m (top of the surface layer). The momentum flux term in Eq. (18) can be omitted when $z_{k+1}$ is greater than 100 meters. In addition, the new parameterization calculates the momentum tendency below the bottom of the rotor area, i.e., only the momentum flux term is retained in Eq. (18).

The variables exchanged between WRF and SWAN is shown in Figure 6. WRF provides 10-m surface wind (U10, V10) to SWAN, whereas SWAN returns SWH (hwave), peak wave length (lwavep), and peak wave period (pwave) to WRF. This variable exchange is implemented in the coupled model. The trained GPR model needs water depth as the input, thus we implement SWAN to provide water depth to WRF. Specifically, we incorporate the GPR model into the surface layer parameterization module of WRF. As a result, the SWH affected by the floating offshore wind turbine (hwavewt) can be calculated directly in the surface layer parameterization module to obtain the roughness length, frictional velocity, and other variables. The frictional velocity at the location of the wind turbine (ustwt) and the frictional velocity unaffected by the turbine (ust) are input to the existing wind farm parameterization module in WRF to make the parameterization module suitable for floating offshore wind farms.

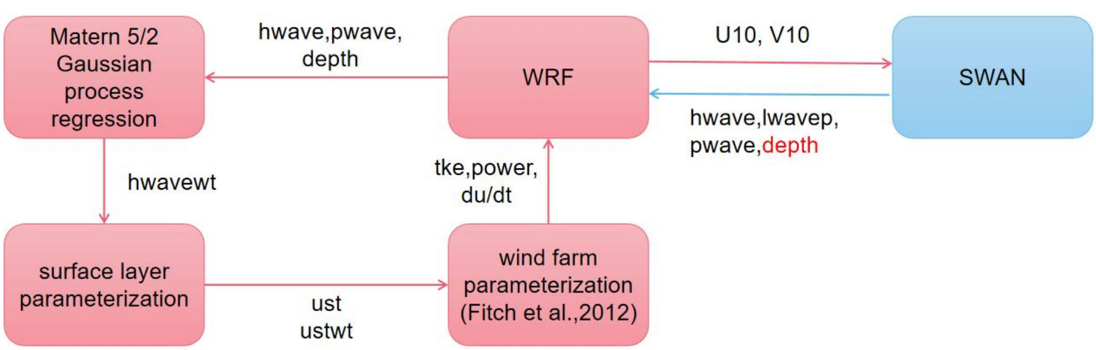


**Figure 6**. Flow chart of floating offshore wind farms parameterization implemented in the coupled model

### 5.2 Model configuration

The model (COAWST, Warner et al., 2010) used to run coupled simulations in this study activates only the atmospheric model (WRFv4.2.2) and the spectral wave model (SWANv41.31).

Initial and lateral boundary conditions for the WRF model are derived from the National Centers for Environmental Prediction FNL Operational Model Global Tropospheric Analyses (temporal resolution: 6-hour, spatial resolution: 1°). The WRF model is configured with 47 vertical levels, where 23 levels are below 1000 m and 15 levels intersect the rotor region. The vertical spacing of the grid on the levels spanned by the wind turbine rotor is approximately 14 m. A single domain with a horizontal resolution of 12 km and a domain size of 275 × 194 grid cells. The major physical parameterization schemes are summarized in Table 1. The wind farm is located in the northern South China Sea where the water depths range from 50 and 63 m (Figure 7a). The distance between the turbines is approximately 1 km. The thrust and power coefficients of the LEANWIND 8 MW reference turbine (LW) are presented in Figure 7b. This floating wind turbine is rated at 8 MW, with a rotor diameter of 164 m, a hub height of 110 m, and a cut-in wind speed of 4 m/s and a cut-out wind speed of 25 m/s (Desmond et al., 2016).

SWAN uses a single domain with 8 km horizontal resolution, which is smaller than the WRF domain in this study. The corresponding parameterization schemes are shown in Table 1. The spectrum is discretized using 24 logarithmically-spaced frequency bins from 0.04 to 1.00 Hz and 36 directional bins with 10° spacing. The boundary conditions are taken from the WaveWatch III (WW3) model (WW3DG, 2019). The nonstationary mode of SWAN is used. The WRF model is coupled with the SWAN model every 10 minutes. The total simulation time is 18 hours (i.e., from 00 UTC on 1 January to 18 UTC on 1 January 2019), with SWAN starting from the initial steady state. A reference simulation (control run, referred as WRF-CTL) is performed without the wind farm. Another simulation (WRF-Fitch) is conducted with the Fitch wind farm parameterization. A third simulation (WRF-FWFP) is performed with the new proposed floating wind farm parameterization.

**Table.1** Physical parameterization schemes used in coupled model.

| | Physics process | Parameterization scheme |
|---|---|---|
| WRF | Microphysics | Single-Moment 6-class (Hong and Lim, 2006; Hong et al., 2006) |
| | Longwave Radiation | Rapid Radiative Transfer Model (Mlawer, 1997) |
| | Shortwave Radiation | Dudhia (Dudhia, 1989) |
| | Surface Layer | MYNN (Nakanishi and Niino, 2009) |
| | Land Surface | thermal diffusion (Duhia, 1996) |
| | Planetary Boundary Layer | Mellor-Yamada-Nakanishi-Niino 2.5-level (Nakanishi and Niino, 2009) |
| | Cumulus | Grell-Freitas ensemble (Grell and Freitas, 2014) |

| | | |
|---|---|---|
| | Roughness | CORE-Talyor-Yelland (Taylor and Yelland, 2001) |
| SWAN | Depth-induced wave breaking | Constant (1.0, 0.73) (Battjes and Janssen, 1978) |
| | Bottom friction | Madsen (0.05) (Madsen et al., 1988) |
| | Wind input | Komen (Komen et al., 1984) |
| | Whitecapping | Komen (Komen et al., 1984) |

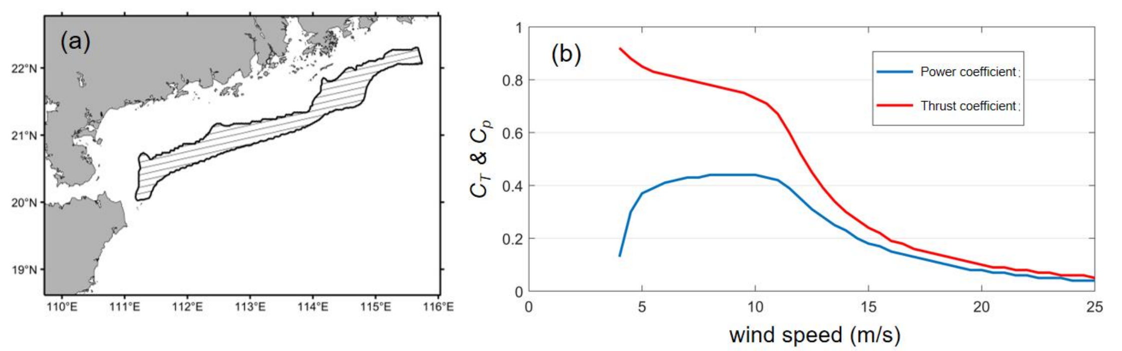


**Figure 7.** (a) location of wind farm (shaded area), (b) the thrust and power coefficients curves of the LW 8 MW wind turbine

### 5.3 Model validation

To validate SWAN results, the simulated SWH is compared with observations of the satellite data Jason-3 (Lillibridge, 2019) (Figure 8). The model is also run for an additional 2 days for further validation. It is evident that the model generally performs well on the wave simulation for the satellite tracks (Pass 38 and Pass 88). The SWH in the model is a bit underestimated on the track Pass 12 and overestimated on the track Pass 51. Generally, the model results have a reasonable performance.

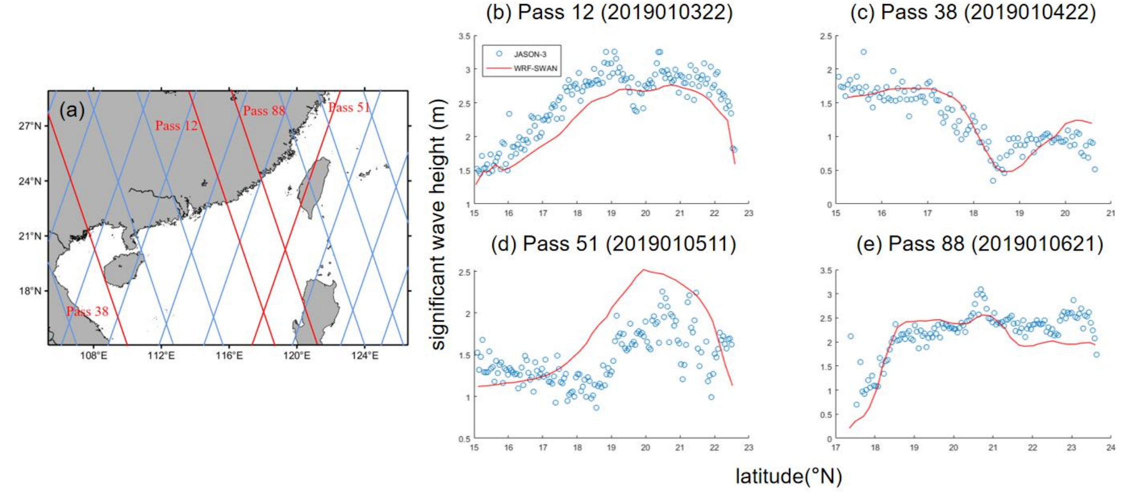

**Figure 8.** (a) Jason-3 gound track from 00 UTC on 1 January to 00 UTC on 7 January in the study region. (b) SWH comparison between model results and Jason-3 data.

### 5.4 Simulation results

In this section, the differences in power output, wind speed deficits, and TKE between the FWFP and Fitch schemes are analyzed in a realistic case using the fully coupled atmosphere-wave model. The last 6 hours of simulations are averaged for all results shown below.

#### 5.4.1 Power output and wind speed deficits

Figure 9 shows that the Fitch scheme underestimates the power output of the entire floating wind farm in the winter scenario, with the difference in power output increasing from the outside of the wind farm to the inside. The power output of a grid cell is underestimated by up to 100 MW (Figure 9a), which means that the power output of a single turbine is underestimated by up to 694 kW (about 144 turbines in a grid cell). The relative difference reaches a maximum of 12 % (Figure 9b), while other regions can reach more than 6 %. FWFP does not directly modify the power output equation in the Fitch scheme. It only modifies momentum tendency terms. However, it should be noted that the change of momentum tendency terms also has a considerable effect on the power output.

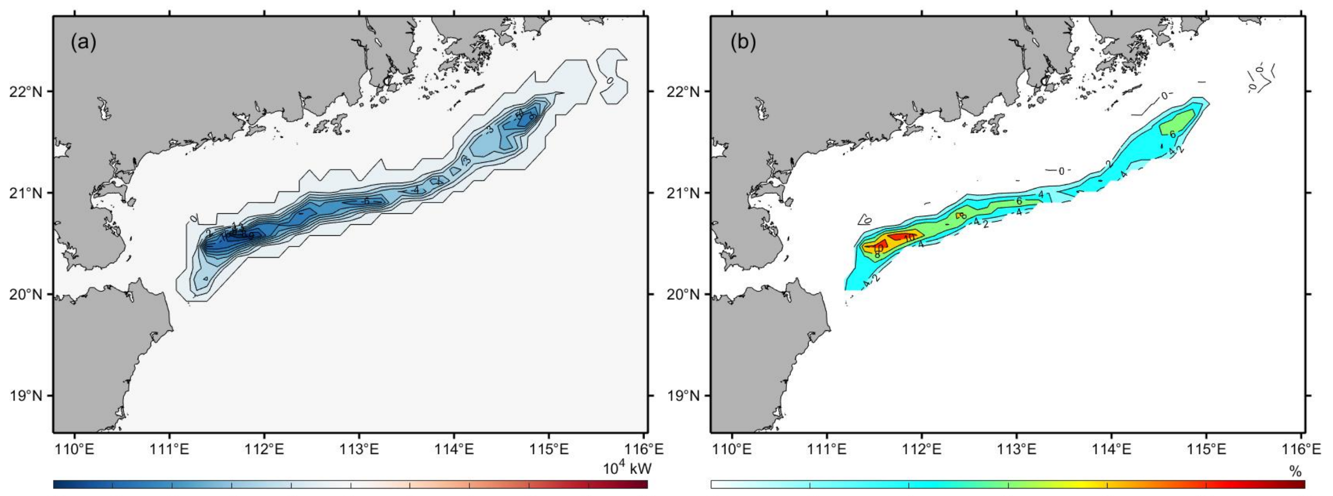


**Figure 9**. (a) Power output differences and (b) relative differences.

The maximum value of momentum reduction at hub height for the FWFP scheme is 6.5 m/s (43 %). Downstream of the wind farm, the wind speed deficit extends into a long wake. From the downstream edge of the wind farm (20.03°N, 111.19° E), the length of the wake reaches 60 km for a wind speed deficit of 2 m/s (13 %). Previous studies found that roughness lengths and turbulence intensity are lower when the subsurface of the atmosphere is oceanic. Therefore, the wake behind offshore wind farms is expected to be much longer than onshore (~50 km) (Emeis et al., 2016; Lundquist et al., 2019). We find that the wind speed deficit at hub height in the WRF-Fitch case is larger than that of the WRF-FWFP (Figure 10b), which helps to explain why the power output is greater in our FWFP scheme. Eq. (21) indicates that the FWFP takes into account the fact that the frictional velocities at the turbine locations are lower at this moment. The FWFP also has a slight impact on the wind-farm wakes.

Vertical profiles of wind speed deficits in WRF-FWFP case also show similar characteristics to WRF-Fitch case. The atmospheric boundary layer (ABL, including downstream) is affected by the wind speed deficit caused by wind farms (Figure 11a). A wind speed deficit of 1 m/s can extend up to the top of the ABL. Figure 11b shows the clear differences that occur within the wind farm, with the Fitch scheme overestimating the wind speed deficit within the ABL compared to the FWFP scheme, which is most pronounced in the rotor area with a maximum value of 0.6 m/s. The top of the turbine to the top of the ABL and the wind-farm wakes also have an effect with values of 0.1 to 0.2 m/s. The difference between the two schemes decreases rapidly at heights above the top of the turbine.

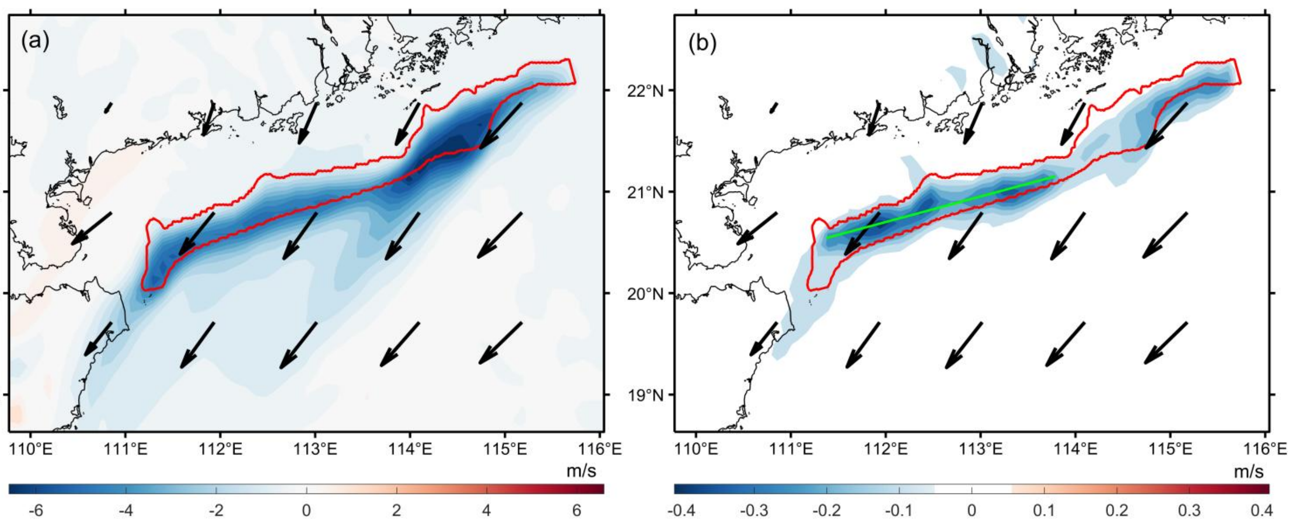


**Figure 10.** Horizontal wind speed differences at the hub height level between (a) WRF-FWFP and WRF-CTL cases and (b) WRF-Fitch and WRF-FWFP cases. The red solid line indicates the outer boundary of the wind farm, and the green solid line indicates a cross section analyzed further.

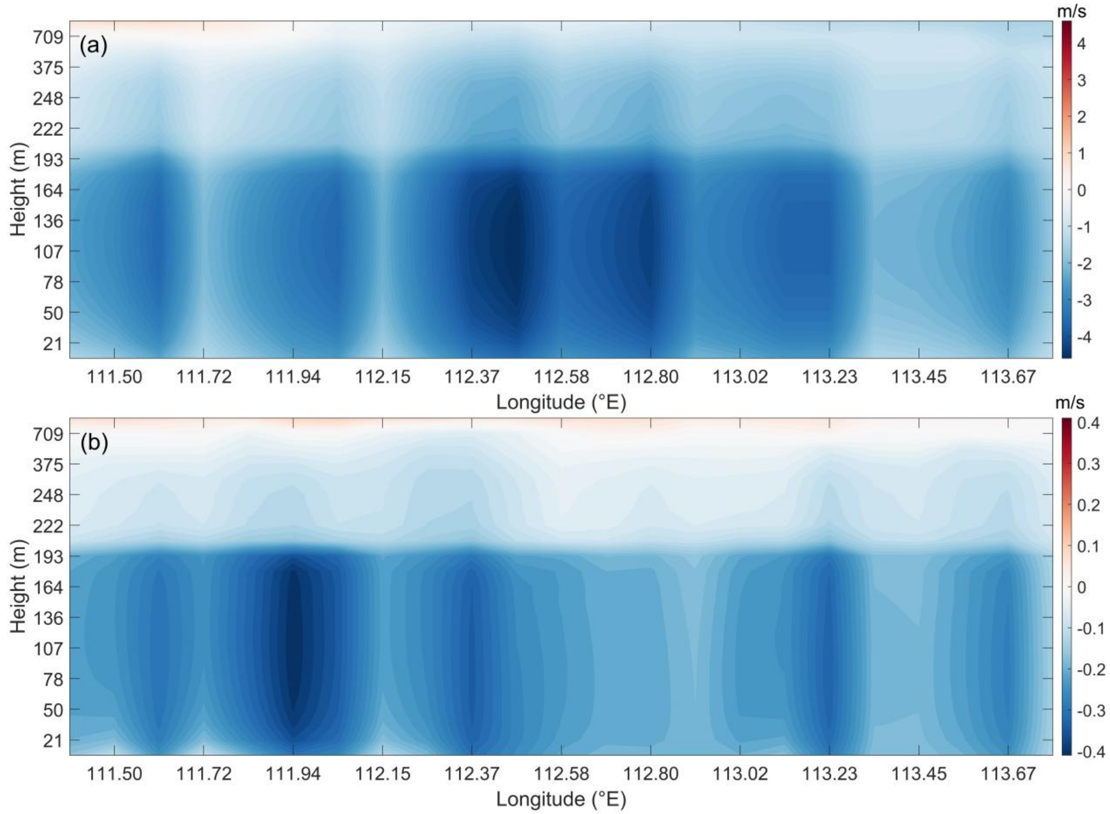


**Figure 11.** Vertical transect of the wind speed differences between (a) WRF-FWFP and WRF-CTL cases and (b) WRF-Fitch and WRF-FWFP cases along the green solid line in Fig.10.

### 5.4.2 TKE

Despite the advection of TKE, it decays rapidly downstream. TKE generated within the wind farm is largely localized within the wind farm area. The maximum increase in TKE at the top of the turbines within the wind farm is 2.4 $m^2 s^{-2}$ (Figure 12a). The WRF-FWFP case produces a smaller TKE within the wind farm compared to the WRF-Fitch case, with a maximum reduction of 0.8 $m^2 s^{-2}$ (Figure 12b). The distribution of horizontal TKE differences is highly similar to that of horizontal wind speed differences (Figure 10b), indicating that the wind shear may dominate the TKE distribution. The reduction in the TKE of 0.3 $m^2 s^{-2}$ continues to extend more than 80 km downstream near the surface (Figure 12c). However, there is little difference in between the WRF-Fitch and the WRF-FWFP in the downstream near the surface (Figure 12d), with most of differences occurring only within the wind farm. The reduction in TKE near the surface in the downstream in WFP-Fitch (Figure 12c) is due to a wind speed deficit and corresponding decrease in wind shear in the lower levels of the wake, resulting in a decrease in shear production in TKE and the reduction in the TKE is no higher than at the top of the turbine (Fitch et al., 2012).

As the wind speeds decrease, the increase in TKE extends to the top of the ABL which is above the wind farm, with an increase of 0.3 $m^2 s^{-2}$ reaching a height of nearly 709 m (Figure 13a). At the top of the turbine, the maximum increase in TKE is 2.4 $m^2 s^{-2}$. Above the top of the turbine, the increase in TKE decreases with height, and below the top of the turbine it increases with height. The difference in TKE between the WRF-Fitch and the WRF-FWFP appears within the local wind farm and is consistent with the location of the difference in wind speeds (Figure 13b). Compared to the WRF-FWFP, WRF-Fitch overestimates the TKE generated throughout the ABL, with the TKE at the top of the wind turbine being the most overestimated (0.4 $m^2 s^{-2}$).

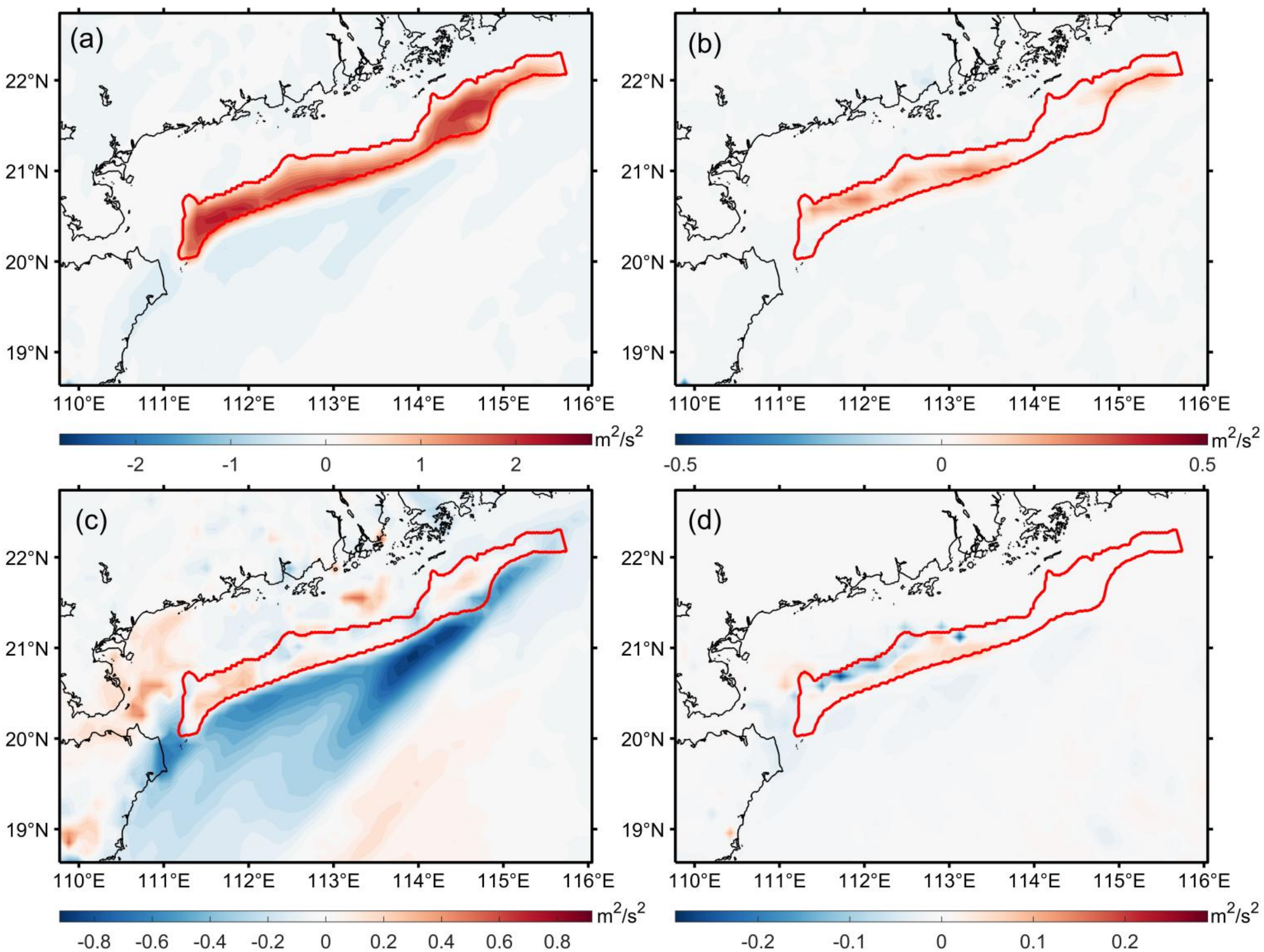


**Figure 12.** Horizontal TKE differences at the top of the turbine between (a) WRF-FWFP and WRF-CTL cases and (b) WRF-Fitch and WRF-FWFP cases, near the surface between (c) WRF-FWFP and WRF-CTL cases and (d) WRF-Fitch and WRF-FWFP cases, and the red solid line shows the outer boundary of the wind farm

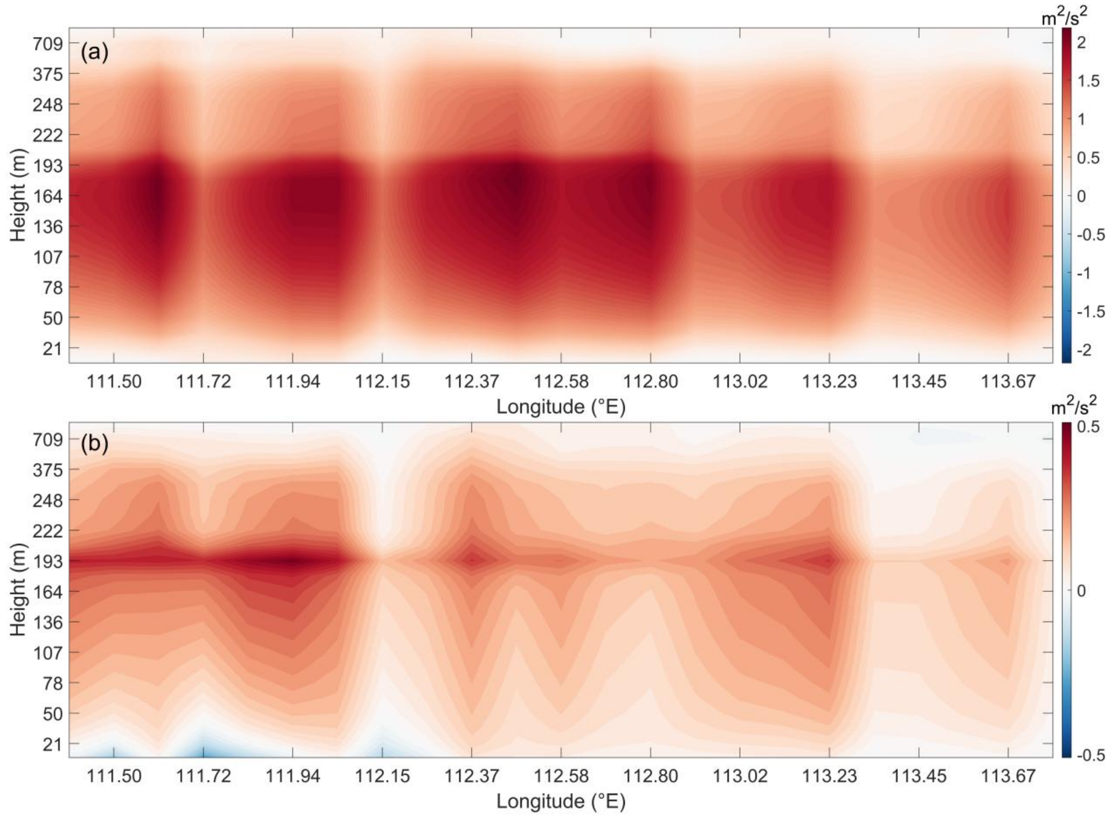


**Figure 13.** The same as in Figure 11, but for TKE

The TKE budget is then examined. In the Planetary Boundary Layer scheme (MYNN 2.5), the TKE is expressed as:

$$\frac{\partial TKE}{\partial t} = P_s + P_b + P_v + P_d, \tag{19}$$

where $P_s$ is the shear production term, $P_b$ is the buoyancy production term, $P_v$ is the vertical transport term, and $P_d$ is the dissipation term. The details about the equations can refer to Janji (2001).

The largest source of the difference in TKE at the top of the turbine is shear generation (Figure 14a), with the TKE at 235 m still making a positive contribution to this difference through vertical transport. The other source is dissipation term, which is the major source of TKE differences in the rotor area. The variation of the near-surface TKE within the wind farm is more complex, with the shear production term, the vertical transport term, and the dissipation term all being important sources, while the TKE generated by the buoyancy term is ignored compared to the other terms (not shown). At the location of 20.59° N, 111.57° E, the vertical shear of the wind speed is not only the largest at the top of the turbine for both WRF-Fitch and the WRF-FWFP, but the difference between the two cases is also the greatest at the top of the turbine (Figure 15). Specifically, the wind shear is 0.056 $s^{-1}$ for WRF-Fitch and 0.0446 $s^{-1}$ for WRF-FWFP. This result can actually be inferred from Figure 11b, which shows that although the maximum value of the difference in wind speed deficit between the two cases is in the rotor area, this difference varies slightly with height, and the height at which the variation with height is most pronounced is at the top of the turbine, followed by the bottom of the rotor area. The smaller wind shear results in the smaller TKE.

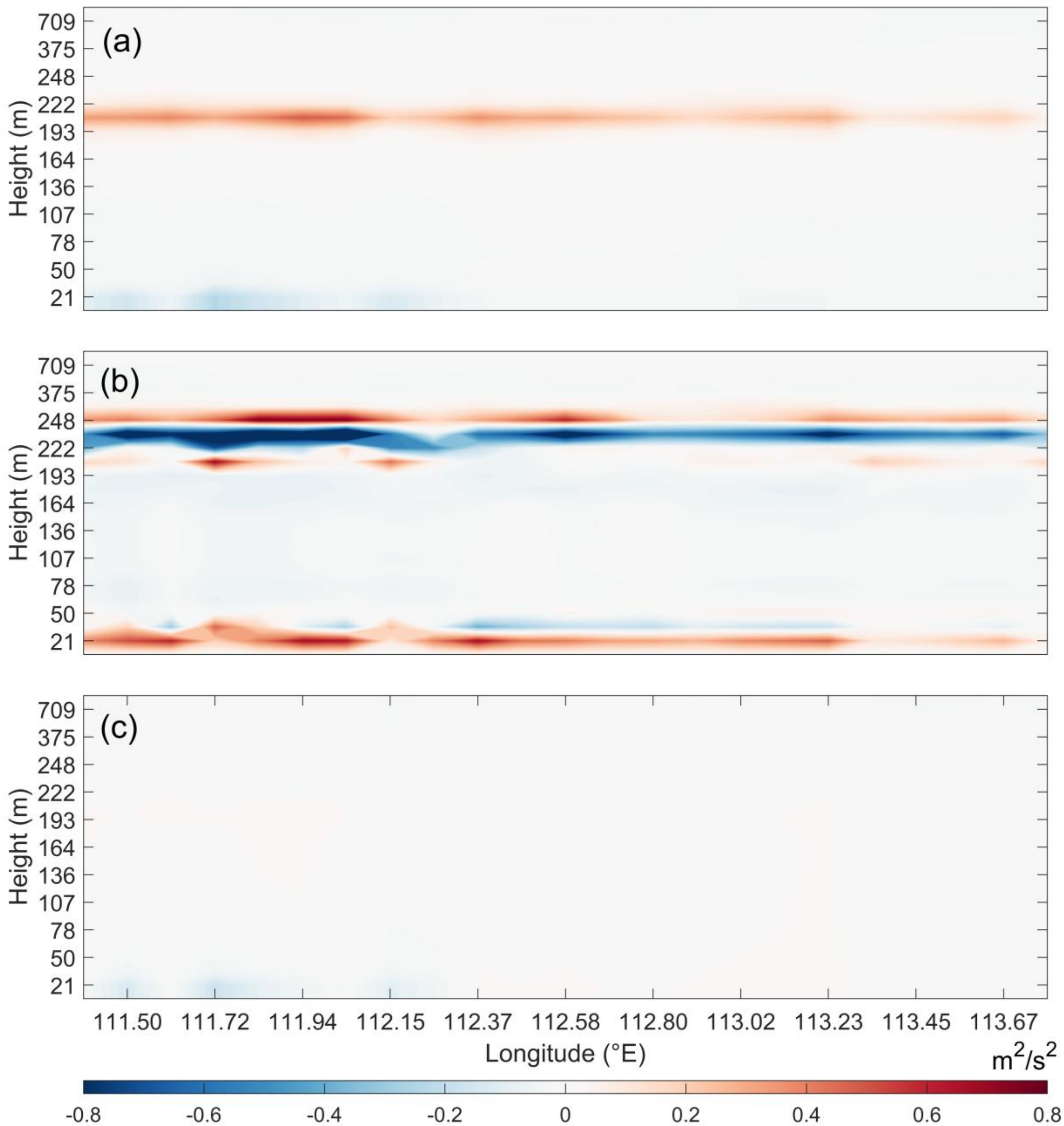


**Figure 14.** Vertical transect of the differences in the TKE budget components between WRF-Fitch and WRF-FWFP cases: (a) shear generation (b) vertical transport (c) dissipation along the green solid line in Fig.10.

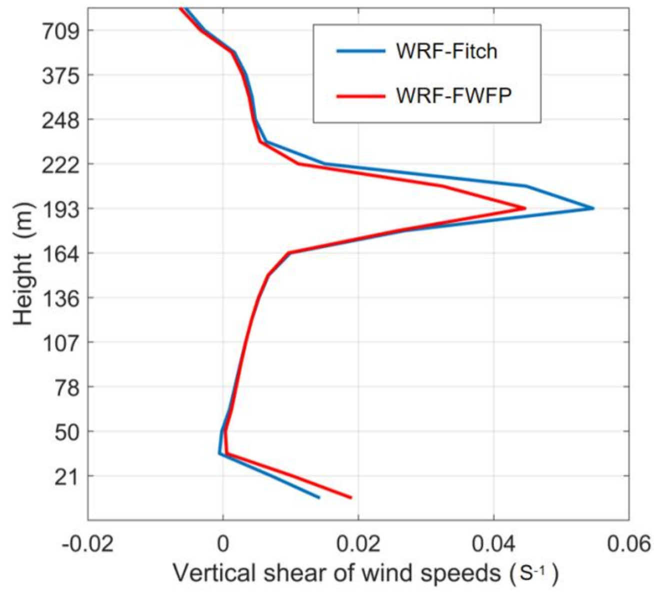


**Figure 15.** Profile of the vertical shear of wind speeds at the location 20.59° N, 111.57° E.

## 6 Conclusions

Floating wind turbines are essential as the offshore wind industry moves into deeper ocean regions. However, current wind farm parameterizations can only be applied to fixed turbines. In this study, we develop a floating wind farm parameterization (FWFP) in a coupled model.

Parameters of the column is modified in the VEG module of SWAN to include the effect of the inertial force to make it suitable for the application of the side column of a floating offshore wind turbine. At the same time, a series of idealized high-resolution SWAN simulations are conducted to investigate the dissipation of wave energy induced by the side columns of floating turbines. It is found that under certain conditions, the side columns of floating turbines can attenuate more than 50 % of the significant wave height (SWH), and a wave "wake" phenomenon occurs with a recovery length of ~1 km. The mean wave direction is also affected, with a symmetrical change of about 5° around the side columns, and the mean wave length increases by more than 20 m. The idealized SWAN simulations and theoretical analyses show that the attenuation of the SWH becomes smaller with the increase of the water depth and is enhanced with the increase of the peak wave period. A total of 660 groups of experiments consisting of different incident SWHs, water depths, and peak wave periods are conducted, and the results of these idealized simulations are used to train a Gaussian process regression (GPR) model with the Matern 5/2 kernel. This model can predict the attenuated SWH due to the side columns of the floating turbine with a given water depth, peak wave period, and incident SWH.

The GPR model is implemented in the WRF and the Fitch wind farm parameterization scheme is modified to form the FWFP. The FWFP modifies the equations for the momentum tendency term because floating structures affect SWH, then the momentum tendency term must also account for changes in surface layer momentum fluxes due to changes in SWH. The difference of the results between the original Fitch scheme and our new FWFP scheme is analyzed in a realistic simulation using a coupled atmosphere-wave model. Results indicate that the Fitch scheme underestimates the power output of the entire floating wind farm in the winter scenario. The power output of a single turbine is underestimated by up to 694 kW (12 %). This is due to the fact that the FWFP scheme takes into account the change in roughness of ocean surface, the Fitch scheme overestimates the wind speed deficit within the wind farm. The impacts spread to the atmospheric boundary layer (ABL) and the wakes, but are most pronounced in in the rotor area, which can be up to 0.6 m/s, suggesting a 15 to 24 % reduction in wind speed deficits. The impact of the FWFP on the turbulent kinetic energy (TKE) near the surface in the downstream of the wind farm is marginal, and it mainly influences the TKE within the wind farm (including the ABL). The Fitch scheme overestimates the TKE generation compared to the FWFP scheme, with the maximum value of 0.4 $m^2\ s^{-2}$ overestimated at the top of the turbine. Because the FWFP diminishes the vertical wind shear at the top of the turbine, which in turn reduces the TKE generated.

Note that a decrease in SWH does not necessarily increase the wind speed in surface layer. In this study, we chose the roughness length parameterization scheme proposed by Taylor and Yelland. (2001), which is a complex iterative computational method where the frictional velocity and roughness length are dependent on each other. The FWFP scheme is only applicable to semi-submersible floating wind turbines because the wind turbine occupying a larger area can induce a significant change in roughness length. In order to better evaluate the power output of floating wind farms and their impacts on the environment, it is necessary to improve the offshore wind farms parameterization.

*Code and Data availability statement.* The NCEP FNL data (NECP, 1999) can be download at website https://rda.ucar.edu/datasets/ds083.0/, wave data (WW3) can be download at https://www.ncei.noaa.gov/thredds-ocean/catalog/ncep/nww3/catalog.html (WW3DG, 2019), and the satellite data (Jason-3) can be obtained from https://www.ncei.noaa.gov/products/jason-satellite-products (Lillibridge, 2019). The coupled model is freely available online (https://github.com/DOI-USGS/COAWST) (Warner et al., 2010). Fortran files related to the offshore wind farms parameterization are available in the public repository (https://osf.io/arj3m/).

*Author contributions.* SD: Methodology, Formal analysis, Investigation, Writing - Original Draft, Writing - Review & Editing; SY: Formal analysis, Writing - Review & Editing; SC: Conceptualization, Funding acquisition, Formal analysis, Investigation, Writing - Review & Editing; XY: Data Curation, Investigation; SC: Investigation.

*Competing interests.* The authors declare that they have no known competing financial interests or personal relationships that could have appeared to influence the work reported in this paper.

*Acknowledgements.* This study is supported by funds from Shenzhen Science and Technology Innovation Committee (WDZC20200819105831001) and the Guangdong Basic and Applied Basic Research Foundation (2022B1515130006). SC is also supported by the Scientific Research Start-up Fund (QD2021021C).

## References

Abkar, M., and Porté-Agel, F. A new wind-farm parameterization for large-scale atmospheric models. Journal of Renewable and Sustainable Energy, 7, 013121. https://doi.org/10.1063/1.4907600, 2015.

Alari, V., and Raudsepp, U. Simulation of wave damping near coast due to offshore wind farms. Journal of Coastal Research, 279, 143－148. https://doi.org/10.2037/41331997, 2012.

AlSam, A., Szasz, R., Revstedt, J. The influence of sea waves on offshore wind turbine aerodynamics. Journal of Energy Resources Technology, Transactions of the ASME, 137, 1-10. https://doi.org/10.1115/1.4031005, 2015.

Battjes, J., and Janssen, J. Energy loss and set-up due to breaking of random waves. Costal Engineering Proceedings, 1, 32. https://doi.org/10.9753/icce.v16.32, 1978.

Booij, N., Ris, R., and Holthuijsen, L. A third-generation wave model for coastal regions: 1. model description and validation. Journal of Geophysical Research: Atmospheres, 104, 7649-7666. https://doi.org/10.1029/98JC02622, 1999.

Dalrymple, R., Kirby, J., and Hwang, P. Wave diffraction due to areas of energy dissipation. Journal of Waterway, Port, Coastal and Ocean Engineering, 110, 67-79. https://doi.org/10.1061/(ASCE)0733-950X(1984)110:1(67), 1984.

Desmond, C., Murphy, J., Blonk, L., and Haans, W. Description of an 8 MW reference wind turbine. Journal of Physics Conference Series, 753, 092013. https://doi.org/10.1088/1742-6596/753/9/092013, 2016.

Diaz, H., and Guedes Soares, C. Review of the current status, technology and future trends of offshore wind farms. Ocean Engineering, 209, 107381. https://doi.org/10.1016/j.oceaneng.2020.107381, 2020.

Du, J., Bolanos, R., and Guo Larsen, X. The use of wave boundary layer model in SWAN. Journal of Geophysical Research: Oceans, 122, 42-62. https://doi.org/10.1002/2016JC012104, 2017.

Dudhia, J. Numerical study of convection observed during the winter monsoon experiment using a mesoscale two-dimensional model. Journal of Atmospheric Sciences, 46, 3077-3107. https://doi.org/10.1175/1520-0469(1989)046<3077:NSOCOD>2.0.CO;2, 1989.

Dudhia, J. A multi-layer soil temperature model for MM5. Sixth PSU/NCAR Mesoscale Model Users Workshop 1996, Boulder, CO, PSU/NCAR, 4950. 1996.

Emeis, S. A simple analytical wind park model considering atmospheric stability. Wind Energy ,13, 459-469. https://doi.org/10.1002/we.367, 2010.

Emeis, S., Siedersleben, S., Lampert, A., Platis, A., Bange, J., Djath, B., et al. Exploring the wakes of large offshore wind farms. Journal of Physics Conference Series, 753, 092014. https://doi.org/10.1088/1742-6596/753/9/092014, 2016.

Fitch, A., Olson, J., Lundquist, J., Dudhia, J., Gupta, A., Michalakes, J., et al. Local and mesoscale impacts of wind farms as parameterized in a mesoscale NWP Model. Monthly Weather Review, 140, 3017-3038. https://doi.org/10.1175/MWR-D-11-00352.1, 2012.

Fitch, A., Olson, J., and Lundquist, J. Parameterization of wind farms in climate models. Journal of Climate, 26, 6439 – 6458. https://doi.org/10.1175/JCLI-D-12-00376.1, 2013.

Fitch, A. Climate impacts of large-scale wind farms as parameterized in a global climate model. Journal of Climate, 28, 6160-6180. https://doi.org/10.1175/JCLI-D-14-00245.1, 2015.

Gettelman, A., Gagne, D., Chen, C., Christensen, M., Lebo, Z., Morrison, H., et al. Machine learning the warm rain process. Journal of Advances in Modeling Earth Systems, 13, e2020MS002268. https://doi.org/10.1029/2020MS002268, 2020.

Grell, G., and Freitas, S. A scale and aerosol aware stochastic convective parameterization for weather and air quality modeling. Atmospheric Chemistry and Physics, 13, 5233-5250. https://doi.org/10.5194/acpd-13-23845-2013, 2013.

Hong, S., and Lim, J. WRF single-moment 6-class microphysics scheme (WSM6). Journal of the Korean Meteorological Society, 42,129-151,2006.

Hong, S., Noh, Y., and Dudhia, J. A new vertical diffusion package with an explicit treatment of entrainment processes. Monthly Weather Review, 134, 2318-2341. https://doi.org/10.1175/MWR3199.1, 2006.

Isaacson, M. Wave-induced forces in the diffraction regime. In: Shwa T L, ed. Mechanics of wave-induced forces on cylinders. London: Pitman Publishing, 68-89, 1979.

Janjic, Z. Nonsingular implementation of the Mellor-Yamada level 2.5 scheme in the NCEP Meso model. NCEP Office note #437 2001;61, 2001.

Jenkins, A., Paskyabi, M., Fer, I., Gupta, A., and Adakudlu, M. Modelling the effect of ocean waves on the atmospheric and ocean boundary layers. Energy Procedia, 24, 166-175. https://doi.org/10.1016/j.egypro.2012.06.098, 2012.

Kalvig, S., Manger, E., Hjertager, B., and Jakobsen, J. Wave influenced wind and the effect on offshore wind turbine performance. Energy Procedia, 53, 202-213. https://doi.org/10.1016/j.egypro.2014.07.229, 2014.

Kobayashi, N., Raichle, A., and Asano, T. Wave attenuation by vegetation. Journal of Waterway, Port, Coastal and Ocean Engineering, 119, 30-48. https://doi.org/10.1061/(ASCE)0733-950X(1993)119:1(30), 1993.

Komen, G., Hasselmann, S., and Hasselmann, K. On the existence of a fully developed wind-sea spectrum. Journal of Physical Oceanography, 14, 1271-1285. https://doi.org/10.1175/1520-0485(1984)014<1271:OTEOAF>2.0.CO;2, 1984.

Lillibridge, John; US DOC/NOAA/NESDIS > Office of Satellite Data Processing and Distribution. Jason-3 Level-2 Operational, Interim and Final Geophysical Data Records (X-GDR), 2016 to present (NCEI Accession 0122595)., 2019.

Lundquist, J., DuVivier, K., Kaffine, D., and Tomaszewski, J. Costs and consequences of wind turbine wake effects arising from uncoordinated wind energy development. Nature Energy, 4, 26-34. https://doi.org/10.1038/s41560-018-0281-2, 2019.

Ma, Y., Archer, C., and Vasel-Be-Hagh, A. Comparison of individual versus ensemble wind farm parameterizations inclusive of sub-grid wakes for the WRF model. Wind Energy, 25, 1573-1595. https://doi.org/10.1002/we.2758, 2022a.

Ma, Y., Archer, C., and Vasel-Be-Hagh, A. The Jensen wind farm parameterization. Wind Energy Science, 7, 2407-2431. https://doi.org/10.5194/wes-7-2407-2022, 2022b.

Madsen, O., Poon, Y., and Graber, H. Spectral wave attenuation by bottom friction: Theory. Proceedings of the 21st International Conference Coastal Engineering, 492-504, 1988.

McCombs, M., Mulligan, R., and Boegman, L. Offshore wind farm impacts on surface waves and circulation in Eastern Lake Ontario. Coastal Engineering, 93, 32-38. https://doi.org/10.1016/j.coastaleng.2014.08.001, 2014.

Mendez, F., and Losada, I. An empirical model to estimate the propagation of random breaking and nonbreaking waves over vegetation fields. Coastal Engineering, 51, 103-118. https://doi.org/10.1016/j.coastaleng.2003.11.003, 2004.

Mlawer, E., Taubman, S., Brown, P., Iacono, M., and Clough, S. Radiative transfer for inhomogeneous atmospheres: RRTM, a validated correlated-k model for the longwave. Journal of Geophysical Research: Atmospheres, 102, 16663－16682. https://doi.org/10.1029/97JD00237, 1997.

Molen, J., Smith, H., Lepper, P., Limpenny, S., and Rees, J. Predicting the large-scale consequence of offshore wind turbine array development on a North Sea ecosystem. Continental Shelf Research, 85, 60-72. https://doi.org/10.1016/j.csr.2014.05.018, 2014.

Morison, J., Johnson, J., and Schaaf, S. The force exerted by surface waves on piles. Journal of Petroleum Technology, 2, 149-154. https://doi.org/10.2118/950149-G, 1950.

Nakanishi, M., and Niino, H. Development of an improved turbulence closure model for the atmospheric boundary layer. Journal of the Meteorological Society of Japan Ser, 87, 895-912. https://doi.org/10.2151/jmsj.87.895, 2009.

NCEP. FNL operational model global tropospheric analyses [Dataset]. NCEP. Retrieved from https://rda.ucar.edu/datasets/ds083.0, 1999.

O'Gorman, P., and Dwyer, J. Using machine learning to parameterize moist convection: Potential for modeling of climate, climate change, and extreme events. Journal of Advances in Modeling Earth Systems, 10, 2548-2563. https://doi.org/10.1029/2018MS001351, 2018.

Pan, Y., and Archer, C. A hybrid wind-farm parametrization for mesoscale and climate models. Boundary-Layer Meteorology, 168, 469-495. https://doi.org/10.1007/s10546-018-0351-9, 2018.

Paskyabi, M., Zieger, S., Jenkins, A., Babanin, A., and Chalikov, D. Sea surface gravity wave-wind interaction in the marine atmospheric boundary layer. Energy Procedia, 53, 184-192. https://doi.org/10.1016/j.egypro.2014.07.227, 2014.

Ponce de León, S., Bettencourt, J., and Kjerstad, N. Simulation of irregular waves in an offshore wind farm with a spectral wave model. Continental Shelf Research, 31, 1541-1557. https://doi.org/10.1016/j.csr.2011.07.003, 2011.

Porchetta, S., Munoz-Esparza, D., Munters, W., Beeck, J., and Lipzig, N. Impact of ocean waves on offshore wind farm power production. Renewable Energy, 180, 1179-1193. https://doi.org/j.renene.2021.08.111, 2021.

Redfern, S., Olson, J., Lundquist, J., and Clack, C. Incorporation of the rotor-equivalent wind speed into the weather research and forecasting model’s wind farm parameterization. Monthly Weather Review, 147, 1029-1046. https://doi.org/10.1175/MWR-D-18-0194.1, 2019.

Roddier, D., Cermelli, C., Aubault, A., and Weinstein A. Wind Float: A floating foundation for offshore wind turbines. Journal of Renewable and Sustainable Energy, 2, 033104. https://doi.org/10.1063/1.3435339, 2010.

Seifert, A., and Rasp, S. Potential and limitations of machine learning for modeling warm-rain cloud microphysical processes. Journal of Advances in Modeling Earth Systems, 12, e2020MS002301. https://doi.org/10.1029/2020MS002301, 2020.

Siedersleben, S., Lundquist, J., Platis, A., Bange, J., Barfuss, K., and Lampert, A., et al. Micrometeorological impacts of offshore wind farms as seen in observations and simulations. Environmental Research Letters, 13, 124012. https://doi.org/10.1088/1748-9326/aaea0b, 2018.

Taylor, P., and Yelland, M. The dependence of sea surface roughness on the height and steepness of the waves. Journal of Physical Oceanography, 31, 572-590. https://doi.org/10.1175/1520-0485(2001)031<0572:TDOSSR>2.0.CO;2, 2001.

Vanderwende, B., and Lundquist, J. Could crop height affect the wind resource at agriculturally productive wind farm sites? Boundary-Layer Meteorology, 158 , 409-428. https://doi.org/10.1007/s10546-015-0102-0, 2016.

Warner, J., Armstrong, B., He, R., and Zambon, J. Development of a coupled ocean-atmosphere-wave-sediment transport (COAWST) modeling system. Ocean Modelling, 35, 230-244. https://doi.org/10.1016/j.ocemod.2010.07.010, 2010.

WW3DG, W. I. D. G. User manual and system documentation of Wavewatch III (R) version 6.07, 2019.

Wu, L., Shao, M., and Sahlée, E. Impact of air-wave-sea coupling on the simulation of offshore wind and wave energy potentials. Atmosphere, 11, 327. https://doi.org/10.3390/atmos11040327, 2020.

Yang, D., Meneveau, C., and Shen, L. Effect of downwind swells on offshore wind energy harvesting-A large-eddy simulation study. Renewable Energy, 70, 11-23. https://doi.org/10.1016/j.renene.2014.03.069, 2014.

Zou, Z., Zhao, D., Zhang, J., Li, S., Cheng, Y., Lv, H., et al. The influence of swell on the atmospheric boundary layer under nonneutral conditions. Journal of Physical Oceanography, 48, 925-936. https://doi.org/10.1175/JPO-D-17-0195.1, 2018.